

Article

Geodynamic Mechanism of the Evolution of the South China Sea Basin: Simulation Based on the Finite Difference Method

Chen Liu ^{1,2,*} and Jianghai Li ^{1,2}¹ School of Earth and Space Sciences, Peking University, Beijing 100871, China; jhli@pku.edu.cn² Key Laboratory of Orogenic Belts and Crustal Evolution, School of Earth and Space Sciences, Peking University, Beijing 100871, China

* Correspondence: 1901110609@pku.edu.cn; Tel.: +86-13366617599

Abstract: The South China Sea is in the convergence zone of the Pacific plate, the Indo-Australian plate, and the Eurasian plate. Its formation and tectonic evolution were influenced by continental margin spreading and plate interaction between the three plates and their microcontinents. It has a complex geodynamic background. To understand how continents break up to form ocean basins, the South China Sea Basin is taken as an example to study the dynamic mechanism of its formation and evolution and the driving force of seafloor spreading, so as to understand the relationship between oceanic–continental lithosphere plates. The South China Sea basin’s opening mechanism and its principal factors of control remain controversial. To explore the influence of different extension rates, we summarized the different genesis mechanisms of the South China Sea, and combined with the tectonic section of the basin, the numerical simulation was obtained based on the finite difference method. The results obtained from numerical simulations show that the rapid extension rate was one of the important factors in the asymmetric expansion of the model, with other factors such as the thickness and rheological properties of the lithosphere held constant. The lithospheric mantle continued thinning in the stress concentration area, with the crust being pulled apart before the lithospheric mantle, eventually forming an ocean basin corresponding to the east sub-basin. However, when the extension rate was low, the model expanded almost symmetrically, and the lithosphere thinning occurred at a slow rate. The simulation results confirm that, compared with the southwest sub-basin of the South China Sea, the spreading rate of the east sub-basin was even higher. We believe that the subduction of the proto-South China Sea played a crucial role in the opening of the South China Sea, providing a more reasonable mechanism. The opposite movement of the Indo-Australian plate and Kalimantan may have inhibited the formation of the southwest sub-basin of the South China Sea, resulting in a later spreading of the southwest sub-basin than the east sub-basin, as well as a lower rate of spreading than the east sub-basin.

Keywords: geodynamic mechanism; South China Sea; extension rate; finite difference method; numerical simulation



Citation: Liu, C.; Li, J. Geodynamic Mechanism of the Evolution of the South China Sea Basin: Simulation Based on the Finite Difference Method. *Appl. Sci.* **2024**, *14*, 1301. <https://doi.org/10.3390/app14031301>

Academic Editor: Andrea L. Rizzo

Received: 30 December 2023

Revised: 2 February 2024

Accepted: 2 February 2024

Published: 4 February 2024



Copyright: © 2024 by the authors. Licensee MDPI, Basel, Switzerland. This article is an open access article distributed under the terms and conditions of the Creative Commons Attribution (CC BY) license (<https://creativecommons.org/licenses/by/4.0/>).

1. Introduction

The South China Sea (SCS) is a Late Cretaceous to Early Miocene marginal sea, which mainly experienced rifting, breaking up, and seafloor spreading under a stretching mechanism during its formation [1,2]. Rifting and seafloor spreading, as two continuous phases of passive continental margin evolution, have recorded different styles of passive margins tectonics in the SCS [3–5]. The northern margin of the SCS is similar to the general continental margin. The lithosphere thinned and extruded toward the ocean, and the basin development and tectonic deformation have also deformed and migrated from the land to the ocean [6]. In the process of seafloor spreading, the proto-South China Sea (PSCS) subduction and the collision between the southern margin and Kalimantan Island have changed the tectonics of the SCS southern margin. This event changed the extension pattern

of the conjugate margin from symmetric to asymmetric [7,8]. The mechanism and structure of the conjugated margin of the east sub-basin (ESB) have revealed a rapid conversion from rift to ocean expansion.

A few models have been developed to explain the formation of the oceanic crust and basins in the SCS. In early studies, the SCS was considered a back-arc basin formed by the back-arc action of the Philippine Sea plate [9,10]. Further research contradicts this view since the back-arc drifting was propelled by the gradual extension of the Philippine Sea plate, and no subduction system was associated with the SCS [11–13]. Then, the paleo-Pacific subduction rollback model was proposed. It is believed that the back-arc stretching was triggered by the Pacific plate subduction [14,15]. The ESB of the SCS was opened in a near N–S direction, and the spreading direction of the SWSB was a NW–SE trend. However, the Pacific plate has been subducted in the NWW direction since the Middle Eocene. The spreading ridge of the SCS is nearly vertical to the Pacific island arc, and the stress patterns do not match [11,16].

Based on the tectonic evolution history of the SCS basin, there are two main widely accepted models: the collision–subduction model [12,17,18] and the collision–extrusion (escape) model [19,20]. The collision–subduction model suggests that the crustal subduction under North Kalimantan Island and the Pacific Ocean plate resulted in the westward opening of the PSCS. In the Late Cretaceous–Miocene period, the PSCS subducted under the Pacific plate and Kalimantan Island and formed an open ocean basin [21,22]. The collision–extrusion (escape) concept implies that the Indian plate moved northward since the Paleocene and collided with the Eurasian plate, which has triggered the strike–slip shear of the main fault zones to support the extrusion movement [12,23–25].

Based on the collision–subduction model, a bidirectional subduction model of the PSCS was established. It suggests that the southern PSCS began to undergo subduction southward in the Early Eocene, and the northern PSCS subducted northward at 30–20 Ma. Seismic tomography also revealed two near-horizontal tabular tomography anomalies under the PSCS and North Kalimantan Island [25,26]. In addition to the above models, the mantle plume model is also considered a possible tectonic model to promote the rupture of the SCS [18,27]. The mantle plume model considers that mantle plume upwelling partially influenced intraplate volcanism in the PSCS spreading and basaltic magmatism at oceanic ridges in the SCS spreading [12,24].

Despite numerous studies of marginal seas and rift basins in the Cenozoic, many unanswered questions remain in the SCS, such as the nature of the rift-to-rupture transition and the extensional patterns of its margins [28,29]. How the South China Sea Basin achieved the rapid transition from tension fracture–rupture–seafloor spreading remains inconclusive. Although many models have been proposed for the opening and evolution of the South China Sea Basin, systematic collation studies have also been conducted [30]. However, it is still not clear how the plates around the South China Sea influenced the formation of the South China Sea basin, and its deep lithospheric dynamics are still unclear. The reasons that led to the extension of the SCS and the change in the direction of the spreading in its later stages, the multistage southward movement of the spreading ridge, and the closure of the SCS are still controversial [31,32].

2. Geological Background

The South China Sea is spread in a NE–SW rhomboid shape, located at 5° N–25° N, 105° E–122° E (Figure 1). The SCS was formed at the convergence of the Pacific, the Indo-Australian, and the Eurasian plates, and it is located in the superposition of the Neo-Tethys (collision) and the Pacific tectonic domain (subduction). A large amount of oceanic lithosphere was subducted into the underlying mantle. Therefore, the SCS basin and its surrounding areas have been subject to intricate tectonic evolution since the Cenozoic, forming a trench–arc–basin ocean–continent subduction system [28,33–35].

The research area has experienced four major stages: the northwesterly extrusion of the Pacific plate (Mesozoic), rifting (Late Cretaceous to Eocene), spreading of the seafloor from

the Oligocene to Middle Miocene, and arc-continental subduction and collision from the Middle Miocene to the present after spreading stopped [4,36]. The northern SCS developed atypical NE–ENE trending dominated passive continental margin rifted basins. The south is mainly a subduction–collision zone with an extrusion basin. The western South China Sea mainly developed the strike-slip pull-apart basins. The east of the SCS developed a N–S trending compressional basin zone. The central part of the SCS basin is a seafloor spreading zone [37,38].

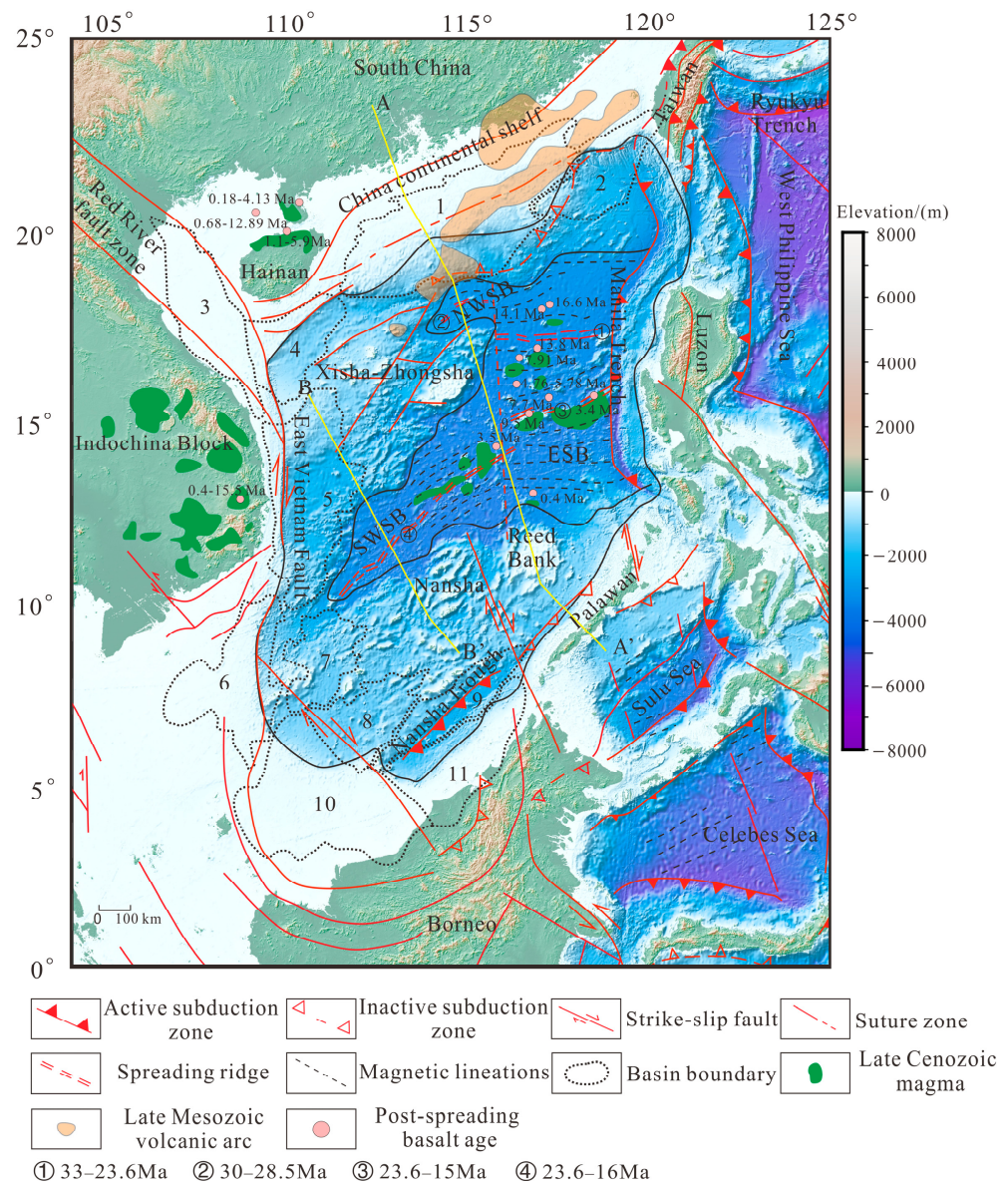


Figure 1. Tectonic map of the South China Sea and its surrounding areas. NWSB: Northwest Sub-basin; SWSB: Southwest Sub-basin; ESB: East Sub-basin; 1: Pearl River Mouth Basin; 2: Southwest Taiwan Basin; 3: Yinggehai Basin; 4: Qiongdongnan Basin; 5: Zhongjiannan Basin; 6: Wan’an Basin; 7: Nanweixi Basin; 8: Beikang Basin; 9: Nansha Trough Basin; 10: Zengmu Basin; 11: Brunei-Sabah Basin. The base map is based on GMT6 [39], Global Bathymetry and Topography at 15 Arc Second: SRTM15+ [40], Mercator projection. Magnetic anomaly strip modified from [41–43]. Late Cenozoic magma modified from [41]. Subduction zones and faults are modified from [44–46]. The two yellow lines are the trace of the geological cross sections provided in Figure 2.

The SCS conjugate mainland margins differed in both N–S and E–W directions [47]. The SCS northern passive margin showed thinned continental crust and aborted oceanic rifting [48], with large co-depositional stratigraphic thicknesses in the northern margin. The southern margin behaved as a typical undercompensated basin. The southern margin lithosphere thickness was much thinner compared to the northern margin [49]. Spatially, the east sub-basin was wider on one side and had strong post-rift magmatism [50], while the SWSB was relatively narrower and had wider continental margins on both sides (Figure 2).

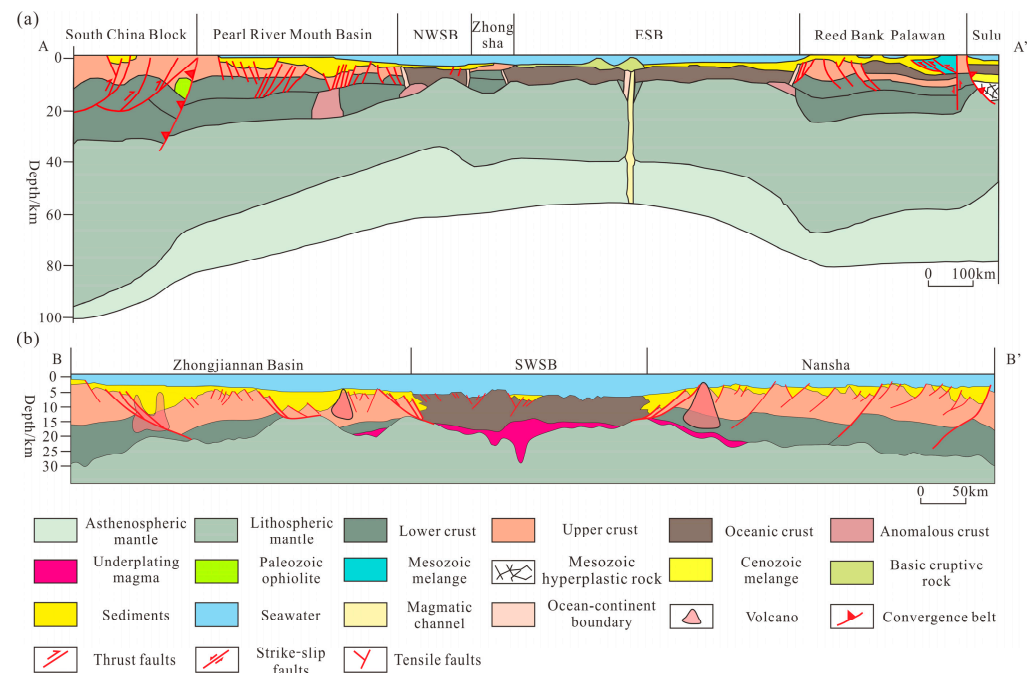


Figure 2. (a) South China Block-Sulu Structural profile map; (b) Southwest sub-basin Structural profile map. Profile (a) Modified according to [51]. Profile (b) Revised according to [49].

The data in Figure 3a are from the Earth magnetic anomaly grid EMAG2 with a resolution of $2' \times 2'$ [52]. The main trend of magnetic anomalies in the South China Sea Basin is N–E and nearly E–W, the trend of magnetic anomalies in the East Sub-basin is nearly E–W, and the trend of magnetic anomalies in the Southwest Sub-basin is NE–SW. The magnetic lineations are approximately parallel to the spreading center of the mid-ocean ridge, which propagated from east to west during the formation of the South China Sea Basin. The oldest identified magnetic lineations are about 32 Ma, and the latest magnetic lineations are about 15.5 Ma [41,42]. The distribution of striped magnetic anomalies (Figure 3) suggests that the SCS basin was formed by a gradual east–west expansion and that the eastern part of the basin began to expand before the western part [53], which began at about 32 Ma and stopped at 15.5 Ma [31]. The former N–S directional spreading formed the Northwest Sub-basin (NWSB) and the East Sub-basin (ESB), and the ESB seafloor spreading began at 29.7 Ma [54]. During this stage, a series of N–S trending pull-apart basins were formed. At ~27–23 Ma, the ESB was characterized by NNW–SSE directional extension. At about 29 Ma and 25 Ma, two southward ridge-jumping events occurred. The spread axis shifted southward, and the Southwest Sub-basin (SWSB) began to expand at 23.6 Ma [55,56]. At approximately 23–15 Ma, the ESB and SWSB continued to expand, and the seafloor spreading ridge changed to a NW–W trend due to the influence of the NNW–W extension [57].

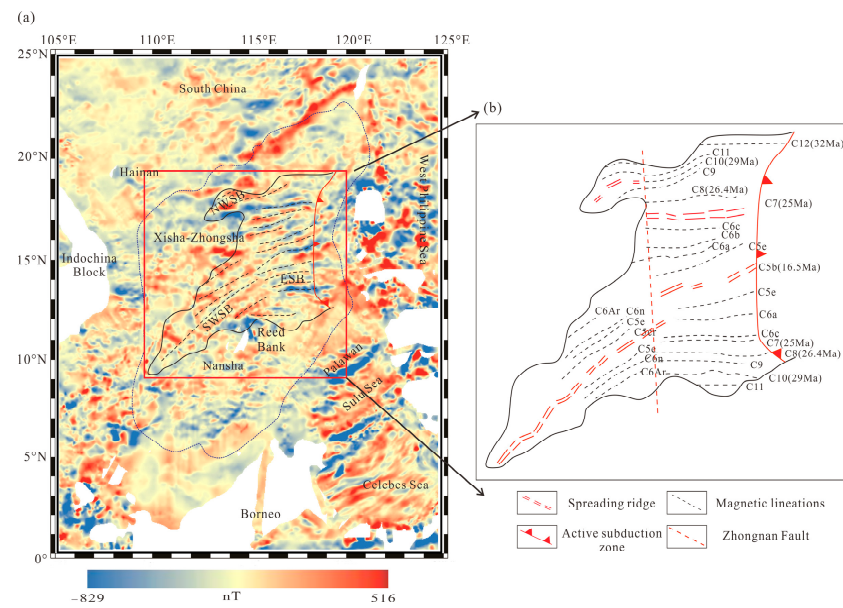


Figure 3. (a) Magnetic anomaly map of the South China Sea basin and its surrounding area [52]; (b) Interpreted magnetic lineations. (b) was modified and supplemented according to references [41,42], and major magnetic anomalies are marked with numbers.

3. Methods and Model Setup

3.1. Methods

The software used in the experiment was MATLAB R2018a. A thermomechanical viscous–elastic–plastic numerical model based on the finite difference method was used to solve the model. The main controlling equations used are [58,59]:

3.1.1. Continuity Equation

In geodynamics, the major rock units (such as the mantle and crust) are considered to be continuous geologic media. The model assumes these geologic media to be incompressible conditions where the material point density does not vary with time:

$$\frac{D\rho}{Dt} = \frac{\partial\rho}{\partial t} + v_i \frac{\partial\rho}{\partial x_i} = 0 \tag{1}$$

$\frac{D\rho}{Dt}$ is the substantive time derivative of density for a moving Lagrangian point, $\frac{\partial\rho}{\partial t}$ is the time derivative of density for the same location’s immobile Eulerian point, v_i is the velocity components.

The incompressible continuity equation can be used for the cases when temperature and pressure do not change greatly and the total volume of the medium does not change. The 2D incompressible continuity equation of mass conservation is:

$$\frac{\partial v_x}{\partial x} + \frac{\partial v_y}{\partial y} = 0 \tag{2}$$

v_x, v_y are components parallel to the respective coordinate axes of the velocity vector \vec{v} .

3.1.2. Momentum Equation

The momentum conservation equation is the equation connecting pressure and deformation, which describes the momentum conservation of the continuum in a gravitational field.

$$\frac{\partial\sigma_{ij}}{\partial x_j} + \rho g_i = \rho \frac{Dv_i}{Dt} \tag{3}$$

With Equation (3) and the relation between the total stress (σ_{ij}) and deviatoric stress (σ'_{ij}), the Navier–Stokes motion equation describing the conservation of momentum for viscous fluid in the gravity field can be obtained:

$$\frac{\partial \sigma'_{ij}}{\partial x_j} - \frac{\partial P}{\partial x_i} + \rho g_i = \rho \frac{Dv_i}{Dt} \quad (4)$$

where ρ is density (kg/m³), P is pressure in units of Pa, g_i is the i -th component of the gravity vector \vec{g} , $\frac{Dv_i}{Dt}$ is the substantive time derivative of the velocity vector (v_i).

3.1.3. Heat Conservation Equation

Heat transport is often intrinsically coupled with deformation. The heat conservation equation (temperature equation) must be derived to predict the temperature change due to heat transfer. This equation (Equation (5)) is nonlinear in T because of the variation in thermal conductivity. Equation (5) describes the heat balance in a continuum media, and it relates temperature changes to thermal generation, conduction, and advection. The Lagrange equation is as follows [60]:

$$\rho C_p \frac{DT}{Dt} = \nabla \cdot (k \nabla T) + \rho H \quad (5)$$

where C_p is heat capacity at constant pressure (J/kg/K), H is volumetric heat production/consumption (W/m³), $\frac{DT}{Dt}$ is the substantive time derivative of temperature, k is the thermal conductivity (W/m/K), ∇ is the divergence operator, ∇T is the gradient of Temperature T .

The thermal conductivity k is based on the following equation [59,61]:

$$k = k_0 + \frac{a}{T + 77} \quad (6)$$

3.1.4. Rock Density and Rheology

The rock density (ρ) depends on the pressure (P), temperature (T), mineralogical composition (M), and chemical composition (C). Using the rules $e^a \approx 1 + a$ and $e^{-a} \approx 1 - a$ (when $a \ll 1$), the equations can be simplified to the following:

$$\rho = \rho_r [1 - \alpha(T - T_r)] \times [1 + \beta(P - P_r)] \quad (7)$$

where ρ_r is the density of a given material at reference pressure P_r ($P_r = 10^5$ Pa in this paper) and temperature T_r ($T_r = 273$ K in this paper), α is the thermal expansion (1/K), and β is the compressibility (1/Pa).

Rheology is the physical property characterizing the flow and deformation behavior of materials [62,63]. In nature, rocks are generally viscous–elastic–plastic. The rheological behavior is based on the minimum creep viscosity by comparing the ductile and brittle/plastic deformation fields [64]. Dry olivine flow laws were used for the asthenospheric mantle and lithospheric mantle, wet quartz flow laws were used for the upper continental crust, and plagioclase An75 flow laws were used for the lower continental crust. The equation used in the calculation was as follows (from the compilation by [64]):

$$\dot{\epsilon}_{II} = A_D (\sigma_{II})^n \exp\left(-\frac{(E_a + V_a P)}{RT}\right) \quad (8)$$

$\dot{\epsilon}_{II}$ is the strain rate, A_D is the material constant, σ_{II} is the deviatoric stress, E_a is activation energy.

The plastic yield strength for a given rock σ_{yield} is based on [65]:

$$\sigma_{yield} = C + \sin(\varphi)P \quad (9)$$

3.2. Model Setup

The initial model set up an ideal undeformed continental lithosphere and simulated its extension under stress. The model did not consider co-deposition and erosion, which could affect lithospheric extension [66]. The model also did not consider the formation of a new oceanic crust at the spreading center, and possible peridotite serpentinization in the oceanic crust region could affect the rheological properties of the rocks [67], which cannot be reflected in the model. This also suggests that there is still a need for subsequent development of more complex models to correspond to the reality.

The setting of the simulation model should be based on the actual situation of the study area. From the Late Cretaceous to the Eocene, the South China Sea was in the continental rift stage, and many sedimentary basins were formed [42]. In the Paleocene–Early Eocene, a continental fluvial–lacustrine depositional system developed in the northern margin of the South China Sea. And littoral and neritic facies clastic rock deposits only occurred in the West Taiwan Basin and Southwest Taiwan Basin. During the Paleocene–Eocene, the basins along the southern margin of the South China Sea mainly developed neritic–hemipelagic facies deposits. During the Late Eocene and Oligocene, the South China Sea began to spread, and the Nansha block separated from the South China block and drifted southeast. In the Early Oligocene, the marine transgression began to occur in the northern margin of the South China Sea, which mainly developed marine–continental interaction facies sandstone and mudstone deposits, and the marine facies in the southern margin of the South China Sea gradually expanded [68].

The drilling data show that the pre-Cenozoic basement has been drilled in the Pearl River Mouth Basin, Qiongdongnan Basin, and Beibuwan Basin at the northern edge of the South China Sea, and the lithology is dominated by granite and metamorphic rocks. The basement of the southern basins of the South China Sea mainly consists of pre-Cenozoic neutral acidic–basic igneous rocks and metamorphic rocks. Among them, the basement of the northeastern continental margin is mainly Mesozoic sedimentary rocks, the northwestern part is Paleozoic metamorphic rocks, the southeastern part is sedimentary rocks, the western land margin is Mesozoic sedimentary rocks, and the southern part is Mesozoic metamorphic rocks [69]. The crustal rocks above the Moho surface are mainly composed of felsic rocks such as gabbro and granulite, while the mantle below the Moho surface is mainly composed of peridotite [67].

The crustal density distribution in the South China Sea region calculated by Li et al. (2022) [70] using the Parker–Oldenburg method is generally distributed in the range of 2700 kg/m^3 to 2900 kg/m^3 , with the density of the South China Sea basins as well as the north and south continental margins above 2800 kg/m^3 , with a higher density in the basin, and the Southwest Taiwan Basin and Palawan Basin showing a lower density below 2760 kg/m^3 , related to the distribution of low-density Mesozoic blocks in this region [70]. The bottom interface of the sedimentary layer is 2670 kg/m^3 [71], and the density of the mantle is about 3300 kg/m^3 [72].

The effective viscosity coefficient of the sedimentary layer in the South China Sea is 10^{22} – $10^{23} \text{ Pa}\cdot\text{s}$, the effective viscosity coefficient of the upper crust varies between 10^{21} and $10^{24} \text{ Pa}\cdot\text{s}$, and from the northern continent to the central basin, the value of η gradually decreases from 10^{24} to $10^{21} \text{ Pa}\cdot\text{s}$, the effective viscosity coefficient of the lower crust varies between 10^{21} and $10^{23} \text{ Pa}\cdot\text{s}$, and the average viscosity of the upper mantle of the rock layer is 10^{20} – $10^{21} \text{ Pa}\cdot\text{s}$ [73]. The average viscosity coefficients of the upper and lower mantle are $10^{19} \text{ Pa}\cdot\text{s}$ and $10^{20} \text{ Pa}\cdot\text{s}$, respectively [74].

The initial model size was $400 \text{ km} \times 250 \text{ km}$ (Figure 4) and was divided into six layers. The top of the model is a sticky layer, it is a weak fluid layer with a low density and low viscosity (viscosity $\eta = 1 \times 10^{18} \text{ Pa}\cdot\text{s}$) [75]. Under the above conditions and with sufficient thickness, the layer interface operates as an internal free surface [76]. Usually, the density of the layer corresponds to either water (1000 kg/m^3) or air (1 kg/m^3). Considering that in the Paleocene–Early Eocene, the continental margin of the South China Sea was mostly fluvial–lacustrine facies and Marine facies, the density of the sticky layer was set at 1000 kg/m^3 .

The initial thickness of the sticky water layer was 10 km. Below the sticky layer, from top to bottom, are the sediment, upper crust, lower crust, lithospheric mantle, and asthenosphere mantle. Zheng et al. (2022) [71] calculated the thickness of the crustal lithosphere, and the normal crust of South China is 30–32 km, the uniform thinning zone of the shelf is about 24–28 km, and the crustal stretching coefficient is less than 1.2 [71], and referring to the cross section of Figure 2, it is assumed that the thickness of the crust before the stretching is about 38 km. Therefore, the thickness of the sediment layer was 2 km, the upper crust was 18 km, the lower crust was 20 km, and the lithospheric mantle was 65 km. The rheological flow law of sedimentary layer was set according to wet quartz [64], the parameters of the rheological flow law of the upper crust were referred to the reference [77,78], the rheological flow law parameters of lower crust were set according to plagioclase An75, and the lithospheric mantle and asthenosphere mantle are dry peridotite [63]. Other parameters of the model were set according to reference [44,59,75,79] and actual geological conditions (Table 1).

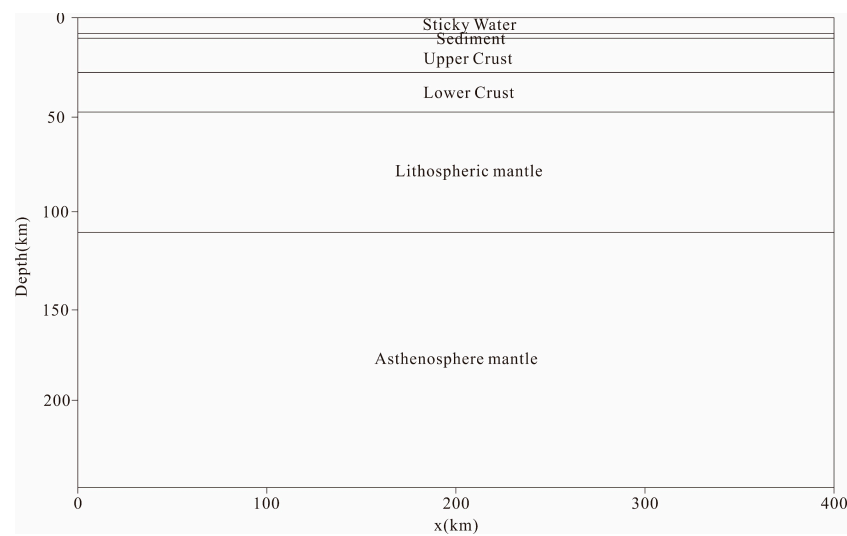


Figure 4. Initial setup of our extension experiments.

Table 1. Basic parameter settings of the South China Sea basin [44,59,75,79].

| | Sticky Layer | Sediment | Upper Crust | Lower Crust | Lithospheric Mantle | Asthenosphere Mantle |
|-------------------------------|---------------------|----------------------|-----------------------|-----------------------|----------------------|----------------------|
| ρ (kg/m ³) | 1000 | 2650 | 2700 | 2800 | 3300 | 3300 |
| n | / | 2.3 | 4 | 3.2 | 3.5 | 3.5 |
| Ea (kJ/mol) | / | 154 | 223 | 238 | 532 | 532 |
| α (1/K) | 2×10^{-5} | 2×10^{-5} | 2×10^{-5} | 2×10^{-5} | 2×10^{-5} | 2×10^{-5} |
| β (1/Pa) | 1×10^{-11} | 1×10^{-11} | 1×10^{-11} | 1×10^{-11} | 1×10^{-11} | 1×10^{-11} |
| A_D (1/s/MPa ⁿ) | / | 3.2×10^{-4} | 1.1×10^{-15} | 5.6×10^{-17} | 2.4×10^{-8} | 1.9×10^{-9} |
| k_0 (W/m/K) | 300 | 0.64 | 0.64 | 1.18 | 0.73 | 0.73 |
| a (W/m) | 0 | 807 | 807 | 474 | 1293 | 1293 |
| C_p (J/kg/K) | 3000 | 1000 | 1000 | 1000 | 1000 | 1000 |
| H_r (W/m ³) | 0 | 2×10^{-6} | 1×10^{-6} | 5×10^{-7} | 2.2×10^{-8} | 2.2×10^{-8} |
| V_a (cm ³) | / | 0 | 0 | 0 | 10 | 10 |
| C_0 | 0 | 1×10^7 | 1×10^6 | 1×10^6 | 1×10^7 | 1×10^7 |
| C_1 | 0 | 1×10^7 | 1×10^6 | 1×10^6 | 1×10^7 | 1×10^7 |

The top boundary of the model had a free-slip condition. Symmetric, horizontally outward, constant velocity boundary conditions were imposed on both sides of the model. The lower lithosphere boundary was not specified. It was a spontaneously formed rheological boundary between the stronger, colder parts of the mantle and the weaker, hotter region below. We used an evolving non-uniformly spaced numerical grid combined with a

time-varying model size in response to imposed bulk extension. The model grid resolution was 161×61 nodes with 120,000 randomly distributed markers.

In the simulation, the temperature at the top of the model was 273 K, and the temperature at the bottom was 1663 K. The adiabatic temperature gradient in the asthenosphere = 0.5 K/km, with an acceleration of gravity $g_y = 9.78 \text{ m/s}^2$. Thermal perturbation in the base of the lithosphere is 10 K.

The full spreading rates of the ESB and the SWSB were 20–80 mm/a and 35–50 mm/a, respectively. The spreading velocity of the ESB was about 70 mm/a during 32–29 Ma. At 29–26 Ma, the spreading rate was about 25 mm/a. The spreading rate remained at about 70 mm/a before the southward transition of 23.6 Ma, and then the spreading rate varied from 50 mm/a to 35 mm/a from 15.5 Ma, which was similar between the ESB and the NWSB [31,80]. The SWSB began spreading around 23.6 Ma and stopped spreading around 16 Ma. Briais et al. (1993) [19] suggested an average expansion rate of 40 mm/a [19], while Barckhausen et al. (2014) [81] proposed a high spreading rate (76–80 mm/a) for the SCS during the final spreading phase [81]. The anomalously thin crust of the SWSB supported a slower spreading rate (half-spreading rate 12.6 mm/a) [82]. If the seafloor spreading rate was close to the extension rate, then the extension rate of the eastern margin may have been significantly faster than that of the western margin. To qualitatively study the magnitude of the extension rate, based on the above data, three sets of models with different extension rates were designed. The constant velocity applied on both sides of the model was half of the extension velocity. The half-extension rates of models 1, 2, and 3 were 30 mm/a, 20 mm/a, and 12.5 mm/a, respectively.

4. Results

We mainly discussed the operation results of three groups of different extensional rate models, their evolution process, and the time of rupture. The original simulation results of the three models (Figures 5–7) were interpreted, and the major faults were marked. In addition, the bulk strain (Figure 8) and viscosity field (Figure 9) changes in models 1 and 2 were compared.

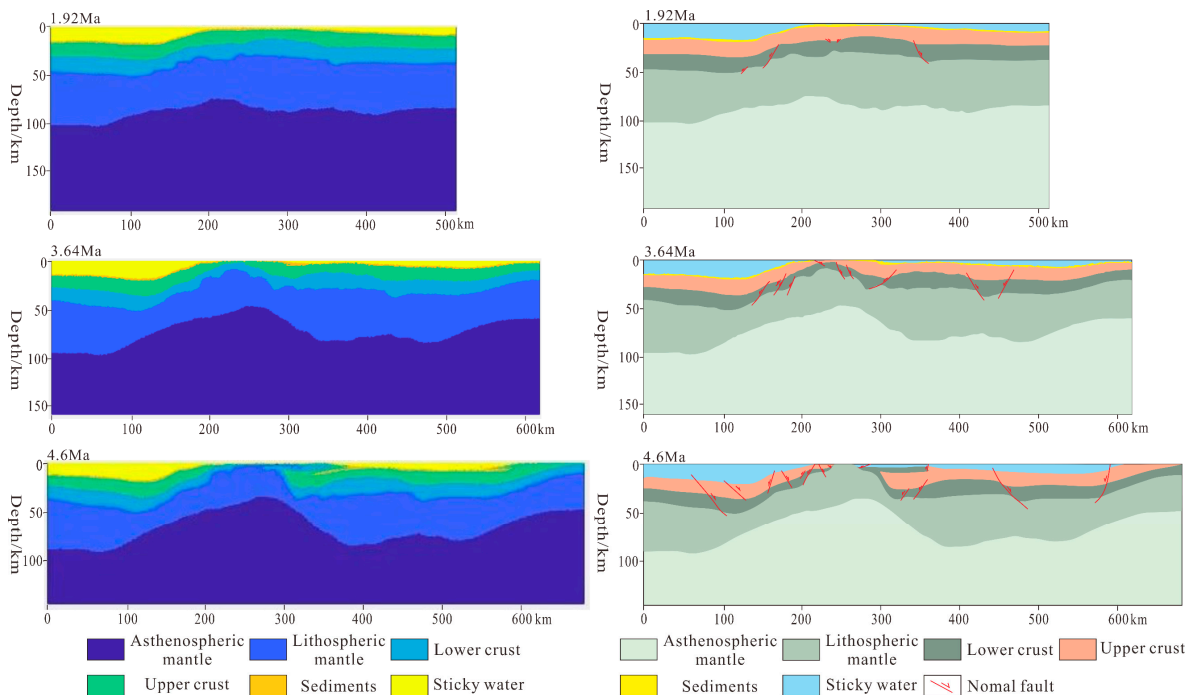


Figure 5. Original simulation results (left) and interpretation (right) of Model 1.

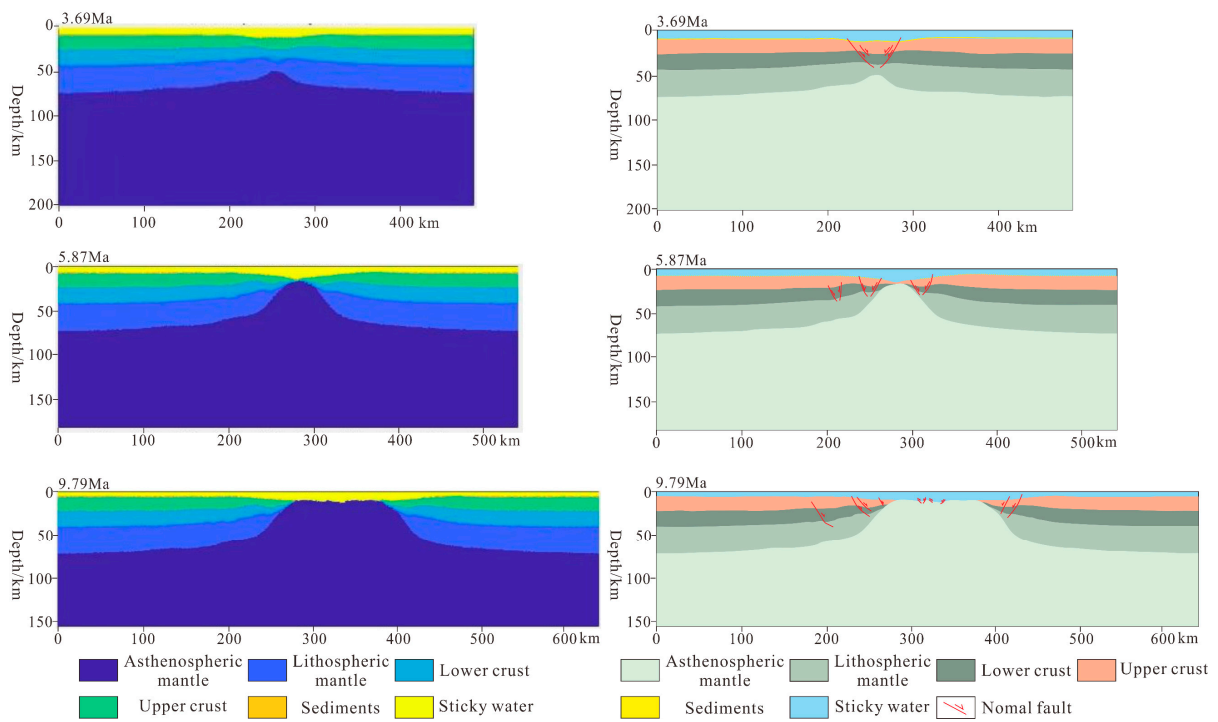


Figure 6. Original simulation results (left) and interpretation (right) of Model 2.

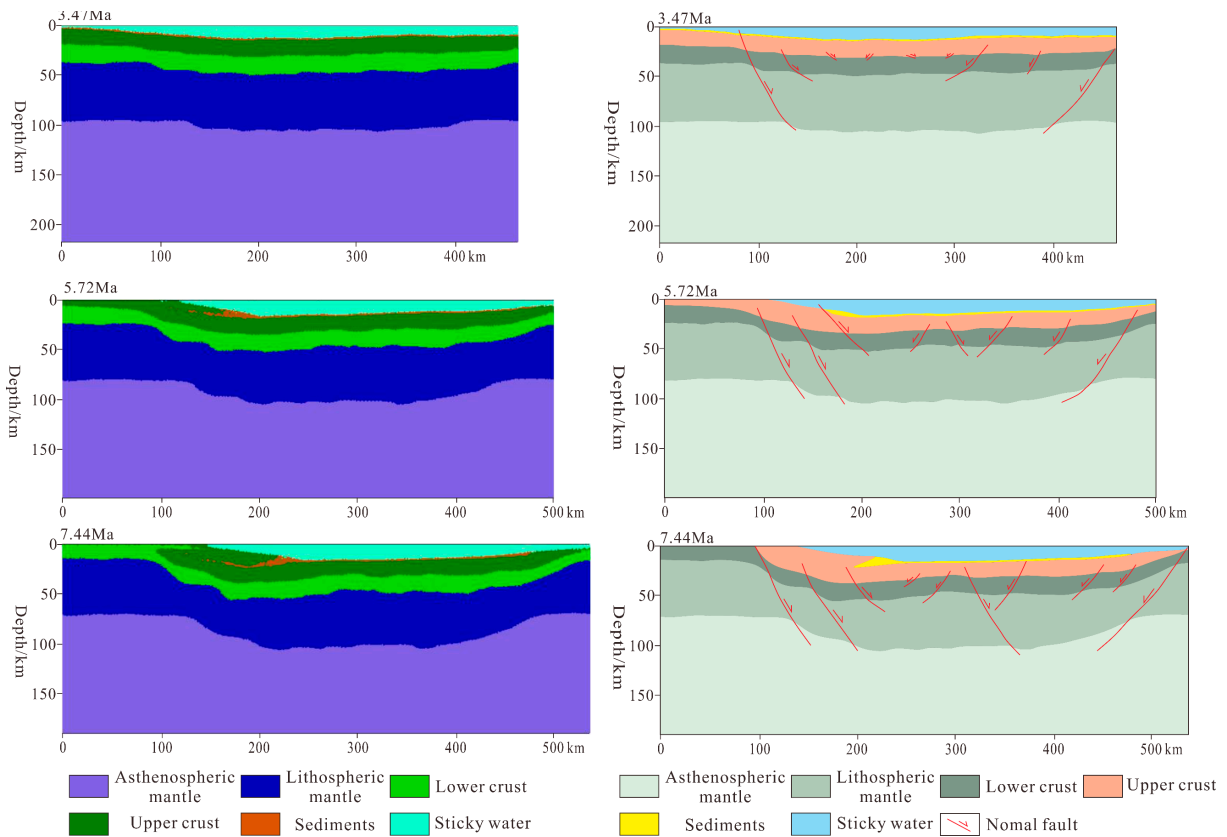


Figure 7. Original simulation results (left) and interpretation (right) of Model 3.

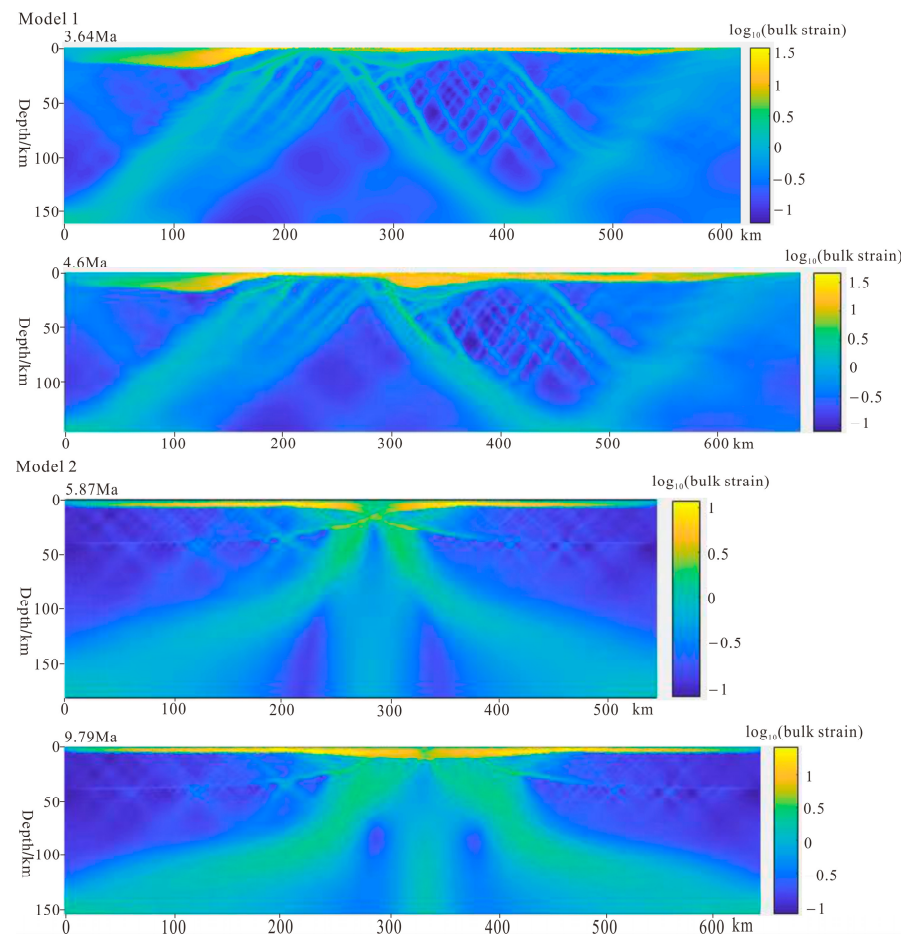


Figure 8. Bulk strain of the simulation results.

Model 1:

In Model 1, the extension rate was fast enough (half-extension rate = 30 mm/a) that, during the initial rift, the lithosphere was thinned rapidly and the mantle upwelled rapidly, heating the lower crust above the Moho temperature and significantly reducing the layer viscosity. Low viscosity in the lower crust led to the decoupling of the mantle and crust, deflecting the mantle upwelling, with the highest heat flux deflected to one margin. The lithospheric mantle continued to thin in the stress concentration area, and the crust was pulled apart before the lithospheric mantle to form the ocean basin (Figure 5). The model presented asymmetric expansion, and the expansion center was closer to the left side of the model, in the area between 200 and 300 km to the left side. Meanwhile, the faults on the left side of the model were relatively dense and large detachment faults, while only a few large normal faults occurred on the right side. It only took 4 Ma from rift development to crustal rupture, which was a short time involving rapid structural development.

In general, the simulation results of Model 1 had a high degree of fitting with profile AA' in Figure 2. The AA' profile exhibits asymmetric spreading, with the size and number of fractures on the northern margin being greater than on the southern. The crustal thickness of the northern margin is slightly greater than that of the southern margin, while the thickness of the lithospheric mantle is smaller in the north than in the south. The results obtained from the simulation of Model 1 are similar to the actual profile, both in terms of the distribution of fractures and the morphology of the crust and lithospheric mantle. Model 1 can initially correspond to the spreading patterns of the NWSB and the ESB.

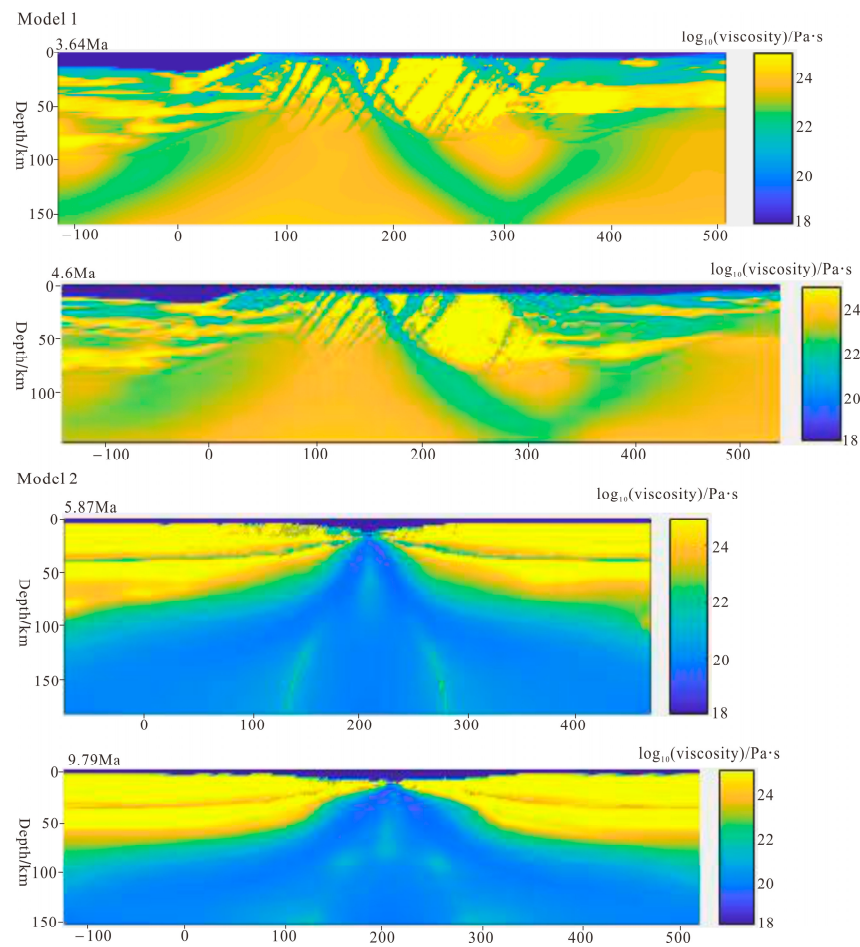


Figure 9. Viscosity of the simulation results.

Model 2:

Model 2 (Figure 6) presented approximately symmetrical spreading, with the spreading center in the center of the model, and the lithospheric mantle and crust fracture occurring almost simultaneously. The resulting faults were mostly concentrated near the spreading center of the model and are symmetrical normal faults. Compared with Model 1, Model 2 had a slower thinning rate, a longer time to reach the final rupture, and a more uniform lithospheric thinning. The faults in Model 2 were smaller in size and did not develop detachment faults, and the geological structure is relatively simpler.

Model 3:

Model 3 (Figure 7) was set up to test the opinion that the SWSB possessed a very slow spreading rate. According to the simulation results, it was found that the lithosphere thinned slowly, and a large number of high-angle normal faults appeared in the model under the condition of a half-extension rate of 12.5 mm/a and formed a nearly symmetrical rift basin. After the model was run for 7.44 Ma, the crust and lithospheric mantle still did not break up, and the thickness of the crust remained large (>10 km), so it was difficult to rupture and form an ocean basin in a short time.

The BB' profile (Figure 2b), the spreading of the southwestern sub-basin, shows nearly symmetrical spreading, with large disruptive faults cutting through the crust and more intense ruptures, and the upper crust of the northern margin has suffered more damage and has thicker sediments than the upper crust of the southern margin. Model 2 (half-extension rate = 20 mm/a) is similar to BB' in that it ruptures the crust over a shorter period of time (<8 Ma) and is nearly symmetrically dilated. Model 3 (half-extension rate = 12.5 mm/a) develops large detachment faults, which are similar to the profile of the SW sub-basin. However, the model has not yet ruptured the crust to form an oceanic basin at 7.44 Ma,

suggesting that this rate is not sufficient to rupture the crust to form an oceanic basin in a short period of time (<8 Ma). Therefore, it is hypothesized that the SW sub-basin expanded at a slower rate (~25 mm/a) during the early stages of spreading and that the rate should have increased slightly during the middle and late stages of spreading, with an average rate of ~40 mm/a. Of course, this may need to be verified by further research by optimizing the velocity sectioning model.

The bulk strain (Figure 8) and viscosity (Figure 9) results can be mirrored with the above simulation results. Compared with models 1 and 2, the higher extension rate led to the rapid mantle flow and earlier rupture time, the strain was more concentrated, and the rheological structure was more complex. In addition, the decrease in crustal viscosity led the mantle to flow and form the rift, and the uplift of the rift side was higher. Moreover, the strain on the right side of Model 1 increased, and the crustal viscosity also decreased, indicating that the rift had a migration trend. The strain of Model 2 was more symmetrical, the strain in the central rift area was the largest, and the typical shear strain could be identified from the middle to the two sides. The rheological structure of Model 2 was simpler, with less variation in crustal viscosity on both sides of the rift. More lithospheric mantle was exhumed at lower extension rates in this study, and exhumation was inversely proportional to the extension rate.

5. Discussion

The South China Sea is a passive continental margin of tensional genesis, which experienced the process of continental margin stretching, rupture, and seafloor spreading during the Late Mesozoic to Early Cenozoic. The crustal structures on the east and west sides of the South China Sea continental margin are significantly different in terms of upper/lower crustal thickness ratio and deformation characteristics [83]. The differences of tectonic activities in the southern and northern margins of the South China Sea are obvious [47]. The genetic mechanism of continental margin extensional basins is closely related to the lithospheric extensional fracture model [84]. The extensional deformation of the lithosphere is the pure shear extensional deformation, forming the basin-ridge-type fault basin system controlled by high-angle normal faults. With the continuous extension, the strength increases and strain concentration occurs, forming large detachment faults. Corresponding to different stages of the evolution of continental margin tensional rupture, the proximal zone, necking zone, distal zone, and ocean–continent transition zone are formed from the land to the ocean [49]. In the initial stages of the rift, the distal and proximal edges of the margin behave differently. In the distal zone of the continental margin, the crust is generally wedge-shaped and brittle, and a large number of extensional detachment faults are developed [85,86].

The northern margin of the South China Sea is similar to the general continental margin. In the early stage of tensional rupture, the distal zone of the northern continental margin generates multiple high-angle normal faults, which control the development of semi-graben or simple graben. With the continuation of extension, some early high-angle faults evolved into large detachment faults, and the lower crust began to be exposed [86,87]. In the process of the SCS underwent expansion, its southern margin was subjected to a southward pulling initiated by the PSCS block subduction, and the collision between Kalimantan Island and the southern margin changed the crustal tectonics in the southern margin, while the northern margin did not [88]. Therefore, the southward flow of the lower crust occurred, which changed the crustal spreading pattern from symmetric to asymmetric. The modification of the late western collision was also limited, and the extension pattern after the collision remained asymmetric. The apparent transformation of the eastern collision shifted the crustal extension pattern from asymmetric to generally symmetric [7].

The passive continental margins are divided into magma-rich type and magma-poor type, and magma plays a decisive role in the process of tensile cracking and rupture of the passive continental margins. Magmatism in the continental margins occurred before the

thinning of the lithosphere [83], and the addition of high-temperature rock veins will lead to the weakening of the rheological structure of the lithosphere, which is conducive to greater deformation of the lithosphere under the same tensile stress. In the process of continental rifting, basaltic magma appeared rapidly in the South China Sea basins, changed from the continental margin to the ocean basin in a short time, and the rupture process was very rapid. The faults at the margins of the South China Sea reflect the close connection between tectonics and magmatism. Similar to other wide rifts, the northern margin of the South China Sea has developed core complex tectonics, which were accompanied by magma intrusion during the extension process. During rifting, the weakening process changed from mechanical weakening along faults to fault localization by serpentinization and magmatism. These melts made the lower crust more ductile, which prevented the strain concentration during the rupture period, resulting in the simultaneous development of multiple detachment faults [86,87].

Many investigations have indicated that the underlying Hainan mantle plume was one of the factors contributing to the expansion of the SCS basin [12,24]. Gao et al. (2023) [57] suggested that some of the magma in the SCS during rifting and initial seafloor spreading originated from the partial melting of the asthenosphere mantle in the northwestern SCS. The Hainan mantle plume probably facilitated the ensuing seafloor spreading and the strong post-spreading magmatism [57]. The ages of trawled basalt samples in the deep basins of the South China Sea are later than the age of the oceanic crust, and the dating results indicate that magmatic activity was mainly concentrated in the late rifting period, especially after the cessation of seafloor spreading [41]. The activity of the mantle plume in Hainan was mainly after the middle Miocene, indicating that rifting and spreading in the South China Sea were not related to the mantle plume. Numerical simulations by Qian et al. (2021) [89] suggested that the Late Cenozoic magmatic activity was not associated with the deep mantle plume but was more compatible with the extensive mantle upwelling generated by the stagnation plate [89].

The early spreading of the conjugate margin in the SCS was asymmetric, with the northern margin having a significantly higher extension rate than the southern margin [90]. The spreading center moved southward in this period until a symmetric oceanic spreading formed after about 28.7 Ma. The full spreading rates of the ESB and the SWSB were 20–80 mm/a and 35–50 mm/a, respectively [31,91]. Yu et al. (2021) [82] proposed that highly faulted and thin oceanic crust was typically produced in slow or ultra-low rate spreading with a spreading rate of less than 40 mm/a [82]. The SWSB of the SCS was similar to the central part of the ESB in having an extraordinarily thin and highly faulted crust. The thin, tectonic crust in the ESB and the SWSB suggests that the final spreading phase, which stopped spreading at 20.5 Ma as proposed by Barckhausen et al. (2014) [81], hardly had a high spreading rate (half-spreading rate 38–40 mm/a) [81]. However, it supported a slower spreading rate (half-spreading rate 12.6 mm/a). The oceanic crust associated with the mantle plume was generally much thicker. However, the thickness of the oceanic crust observed at the ESB Center was only 3.7–6.0 km, and the original crust should have been thinner. Therefore, the magmatic contribution of the Hainan mantle plume during the final extension to the post-extensional phase may have been very limited [82].

The formation and tectonic evolution were influenced by continental margin spreading and plate interaction between the three plates and their microcontinents [92]. In the western and southern parts of the South China Sea, the Indo-Australian plate drifts and subducts northward, while in the east, the Pacific and the Philippine plates drift and subduct north-westward [93]. Based on the tectonic evolution history of the SCS basin, there are several models to explain the formation of the South China Sea. (1) Back-arc extension model [30,94]: The model suggests that the extension and opening of the Southeast Asian back-arc basin is the result of the oblique subduction of the Paleo-Pacific Ocean and the migration of the subduction zone to the ocean. (2) The collision–subduction model [12,17,18]: The model suggests that subduction of the crust under the North Kalimantan and Pacific plates led to the westward opening of the proto-South China Sea. In the Late Cretaceous–Miocene, the

PSCS subducted under the Pacific plate and Kalimantan Island [95] and formed an open ocean basin. (3) The collision–extrusion (escape) model [19,20]: The model implies that the Indian plate moved northward since the Paleocene and collided with the Eurasian plate, which has triggered the strike–slip shear of the main fault zones to support the extrusion movement [12,23–25]. (4) A bidirectional subduction model of the PSCS [25,26]: Seismic tomography also revealed two near-horizontal plate tomography anomalies under the South China Sea and North Kalimantan, and it is believed that bi-directional subduction occurred in the PSCS and that bi-directional subduction of the PSCS contributed to the opening of the South China Sea. (5) The mantle plume model [18,27]: The mantle plume model suggests that the volcanism before the spreading of the South China Sea and the basaltic magmatism in the ocean ridge during the spreading of the South China Sea are partly influenced by the outpouring of mantle plumes.

According to the measured geophysical data, the extension rate of the SCS's northern margin was significantly higher than that of the southern margin, which was one of the important reasons for the N–S tectonic inconsistency of the SCS basin. The numerical simulation results in this paper also show that lithospheric extension and thinning could be produced without the need for a mantle plume, as the results could be obtained by changing the extension rate alone without the addition of a mantle plume. The simulation results confirm that, compared with the Southwest Sub-basin of the South China Sea, the spreading rate of the East Sub-basin was even higher. Model 1 can initially correspond to the spreading patterns of the NWSB and ESB, and it is believed that the extension rate of the ESB is about 60 mm/a. According to Model 2 and Model 3, it is hypothesized that the SW sub-basin expanded at a slower rate (~25 mm/a) during the early stages of spreading and that the rate should have increased slightly during the middle and late stages of spreading, with an average rate of ~40 mm/a.

Therefore, we can infer that the eastern part of the South China Sea has a higher driving force than the western part in the process of opening, and the eastern basin formed earlier than the western basin. The mutual movement of the plates promoted the subduction of the proto-South China Sea, played a crucial role in the opening of the South China Sea, and provided a reasonable mechanism. The collision between the Indo-Australian plate and the Eurasian plate led to the continuous southward extrusion of the Indochina block, while Kalimantan drifted northward and rotated counterclockwise by nearly 60°. The opposite movement of the Indochina block and Kalimantan may have inhibited the formation of the southwest sub-basin of the South China Sea, resulting in the spreading time of the southwest sub-basin being later than that of the east sub-basin, and the extension rate being lower than that of the east sub-basin. The sinistral strike–slip of the Red River fault zone, which accompanied the collision between the Indo-Australian plate and the Eurasian plate, also had a certain impact on the opening of the South China Sea, which may have prompted the change in the basin extension direction.

6. Conclusions

Numerical simulations show that the tectonic asymmetry of the South China Sea basin was influenced by the extension rate, which can affect the rock rheology, produce different structures, and control the migration of ocean ridges. The rapid expansion rate was one of the important factors in the asymmetric expansion of the model, with other factors held constant. With rapid lithospheric extension thinning and mantle upwelling, the lower crust was heated above the Moho temperature, and the layer viscosity was significantly reduced. The lower crust of low viscosity decoupled the mantle and crust, deflecting the mantle upwelling, resulting in the thinning and the highest heat flux towards one margin. The lithospheric mantle continued thinning in the stress concentration area, with the crust being pulled apart before the lithospheric mantle, eventually forming an ocean basin. However, when the extension rate was low, the model expanded almost symmetrically, and the lithosphere thinning occurred at a slow rate.

The simulation results of Model 1 are relatively similar to the actual profile in Figure 2a. This indicates that the east sub-basin and the northwest sub-basin have higher extension rates (~60 mm/a). Model 2 showed nearly symmetrical spreading, with the center of spreading located in the center of the model, and the lithosphere ruptured to form an oceanic basin, and the resulting faults were mostly concentrated near the center of the model spreading, and were symmetrical normal faults. In Model 3, the lithosphere thinned slowly, and a large number of high-angle normal faults appeared in the model, forming a nearly symmetrical rift basin, and no ocean basin was formed. Model 2 resulted in the formation of an ocean basin within a short time (<8 Ma) of lithospheric rupture, and Model 3 developed large detachment faults, which were similar to the actual situation of the SWSB, respectively. Therefore, it is hypothesized that the SWSB expanded at a slower rate (~25 mm/a) during the early stages of spreading and that the rate should have increased slightly during the middle and late stages of spreading, with an average rate of ~40 mm/a. This also proves that the spreading rate of the SCS's ESB was faster than that of the SWSB.

We believe that the subduction of the proto-South China Sea played a crucial role in the opening of the South China Sea, providing a more plausible mechanism. The opposite movement of the Indo-Australian plate and Kalimantan may have inhibited the formation of the southwest sub-basin of the South China Sea, resulting in a later spreading of the southwest sub-basin than the east sub-basin, as well as a lower rate of spreading than the east sub-basin.

Author Contributions: Conceptualization, C.L.; methodology, C.L.; software, C.L.; validation, C.L.; investigation, C.L. and J.L.; data curation, C.L.; writing—original draft preparation, C.L. and J.L.; writing—review and editing, C.L. All authors have read and agreed to the published version of the manuscript.

Funding: This research was funded by the National Key Research and Development Program of China, grant number 2023YFC2906501 and the China National Science and Technology Major Project, grant number 2016ZX05033001.

Institutional Review Board Statement: Not applicable.

Informed Consent Statement: Not applicable.

Data Availability Statement: Data are contained within the article.

Acknowledgments: The simulation in this paper was carried out using MATLAB, and the code used was modified from Gerya (2019). The base map in Figure 1 was generated using GMT6. I would like to express my sincere thanks here.

Conflicts of Interest: The authors declare no conflict of interest.

References

1. Larsen, H.C.; Mohn, G.; Nirrengarten, M.; Sun, Z.; Stock, J.; Jian, Z.; Klaus, A.; Alvarez-Zarikian, C.A.; Boaga, J.; Bowden, S.A.; et al. Rapid transition from continental breakup to igneous oceanic crust in the South China Sea. *Nat. Geosci.* **2018**, *11*, 782–789. [[CrossRef](#)]
2. Wang, P.X. Exploring the deep sea processes in the South China Sea. *Sci. Technol. Rev.* **2020**, *38*, 6–20. (In Chinese) [[CrossRef](#)]
3. Franke, D.; Savva, D.; Pubellier, M.; Steuer, S.; Mouly, B.; Auxietre, J.; Meresse, F.; Chamot-Rooke, N. The final rifting evolution in the South China Sea. *Mar. Pet. Geol.* **2014**, *58*, 704–720. [[CrossRef](#)]
4. Wang, P.C.; Li, S.Z.; Suo, Y.H.; Guo, L.L.; Wang, G.Z.; Hui, G.G.; Santosh, M.; Somerville, D.; Cao, X.Z.; Li, Y. Plate tectonic control on the formation and tectonic migration of Cenozoic basins in northern margin of the South China Sea. *Geosci. Front.* **2020**, *11*, 1231–1251. [[CrossRef](#)]
5. Wen, Y.L.; Li, C.F.; Wang, L.J.; Liu, Y.T.; Peng, X.; Yao, Z.W.; Yao, Y.J. The onset of seafloor spreading at the northeastern continent-ocean boundary of the South China Sea. *Mar. Pet. Geol.* **2021**, *133*, 105255. [[CrossRef](#)]
6. Pang, X.; Zheng, J.Y.; Mei, L.F.; Liu, B.J.; Zhang, Z.T.; Wu, Z.; Feng, X. Characteristics and origin of continental marginal fault depressions under the background of preexisting subduction continental margin, northern South China Sea, China. *Pet. Explor. Dev. Online* **2021**, *48*, 1237–1250. [[CrossRef](#)]
7. Bai, Y.L.; Wang, X.Y.; Dong, D.D.; Brune, S.; Wu, S.G.; Wang, Z.J. Symmetry of the South China Sea conjugate margins in a rifting, drifting and collision context. *Mar. Pet. Geol.* **2020**, *117*, 104397. [[CrossRef](#)]

8. Luo, X.G.; Wang, W.Y.; Zhang, G.C.; Zhao, Z.G.; Liu, J.L.; Xie, X.J.; Qiu, Z.Y.; Feng, X.L.; Ji, X.L.; Wang, D.D. Study on distribution features of faults based on gravity data in the South China Sea and its adjacent areas. *Chin. J. Geophys.* **2018**, *61*, 4255–4268. (In Chinese) [[CrossRef](#)]
9. Avraham, B.Z.; Uyeda, S. The evolution of the China Basin and the mesozoic paleogeography of Borneo. *Earth Planet. Sci. Lett.* **1973**, *18*, 365–376. [[CrossRef](#)]
10. Karig, D.E. Origin and development of marginal basins in the western Pacific. *J. Geophys. Res.* **1971**, *76*, 2542–2561. [[CrossRef](#)]
11. Jiang, X.; Wang, Z.C. A critical review of existing models for the origin of the South China Sea and a new proposed model. *J. Asian Earth Sci.* **2021**, *6*, 100065. [[CrossRef](#)]
12. Li, J.B.; Ding, W.W.; Lin, J.; Xu, Y.G.; Kong, F.S.; Li, S.Z.; Huang, X.L.; Zhou, Z.Y. Dynamic processes of the curved subduction system in Southeast Asia: A review and future perspective. *Earth-Sci. Rev.* **2021**, *217*, 103647. [[CrossRef](#)]
13. Taylor, B.; Karner, G.D. On the evolution of marginal basins. *Rev. Geophys.* **1983**, *21*, 1727–1741. [[CrossRef](#)]
14. Morley, C.K. Late Cretaceous–Early Palaeogene tectonic development of SE Asia. *Earth Sci. Rev.* **2012**, *115*, 37–75. [[CrossRef](#)]
15. Stern, R.J.; Bloomer, S.H. Subduction zone infancy: Examples from the Eocene Izu-Bonin-Mariana and Jurassic California arcs. *Geol. Soc. Am. Bull.* **1992**, *104*, 1621–1636. [[CrossRef](#)]
16. Huang, C.Y.; Wang, P.X.; Yu, M.M.; You, C.F.; Liu, C.S.; Zhao, X.X.; Shao, L.; Zhong, G.F.; Yumul, G.P. Potential role of strike-slip faults in opening up the South China Sea. *Natl. Sci. Rev.* **2019**, *6*, 891–901. [[CrossRef](#)] [[PubMed](#)]
17. Holloway, N.H. North Palawan Block, Philippines; its relation to Asian mainland and role in evolution of South China Sea. *AAPG Bull.* **1982**, *66*, 1355–1383. [[CrossRef](#)]
18. Cao, L.C.; Shao, L.; Qiao, P.J.; Cui, Y.C. Formation and paleogeographic evolution of the Palawan continental terrane along the Southeast Asian margin revealed by detrital fingerprints. *Geol. Soc. Am. Bull.* **2020**, *133*, 1167–1193. [[CrossRef](#)]
19. Briais, A.; Patriat, P.; Tapponnier, P. Updated interpretation of magnetic anomalies and seafloor spreading stages in the south China Sea: Implications for the Tertiary tectonics of Southeast Asia. *J. Geophys. Res.* **1993**, *98*, 6299–6328. [[CrossRef](#)]
20. Tapponnier, P.; Peltzer, G.; Armijo, R. On the mechanics of the collision between India and Asia. *Geol. Soc. Lond. Spec. Publ.* **1986**, *19*, 113–157. [[CrossRef](#)]
21. Hall, R. Cenozoic geological and plate tectonic evolution of SE Asia and the SW Pacific: Computer-based reconstructions, model and animations. *J. Asian Earth Sci.* **2002**, *20*, 353–431. [[CrossRef](#)]
22. Hall, R. Late Jurassic-Cenozoic reconstructions of the Indonesian region and the Indian Ocean. *Tectonophysics* **2012**, *570–571*, 1–41. [[CrossRef](#)]
23. Hall, R.; Breitfeld, H.T. Nature and demise of the proto-South China Sea. *Bull. Geol. Soc. Malays.* **2017**, *63*, 61–76. [[CrossRef](#)]
24. Burton-Johnson, A.; Cullen, A. Continental rifting in the South China Sea through extension and high heat flow: An extended history. *Gondwana Res.* **2023**, *120*, 235–263. [[CrossRef](#)]
25. Wu, J.; Suppe, J. Proto-South China Sea plate tectonics using subducted slab constraints from tomography. *J. Earth Sci.* **2018**, *29*, 1304–1318. [[CrossRef](#)]
26. Lin, J.; Sun, Z.; Li, J.B.; Zhou, Z.Y.; Zhang, F.; Luo, Y.M. South China Sea basin opening: Lithospheric Rifting and Interaction with Surrounding Subduction Zones. *Sci. Technol. Rev.* **2020**, *38*, 35–39. (In Chinese) [[CrossRef](#)]
27. Mai, H.A.; Chan, Y.L.; Yeh, M.W.; Lee, T.Y. Tectonic implications of Mesozoic magmatism to initiation of Cenozoic basin development within the passive South China Sea margin. *Int. J. Earth Sci.* **2018**, *107*, 1153–1174. [[CrossRef](#)]
28. Wang, P.C.; Li, S.Z.; Suo, Y.H.; Guo, L.L.; Santosh, M.; Li, X.Y.; Wang, G.Z.; Jiang, Z.X.; Liu, B.; Zhou, J.; et al. Structural and kinematic analysis of Cenozoic rift basins in South China Sea: A synthesis. *Earth-Sci. Rev.* **2021**, *216*, 103522. [[CrossRef](#)]
29. Wang, Z.C.; Li, J.H.; Feng, Z.Q.; Wang, L.J.; Liu, C. Mechanism of Structure Variations at Rifted Margins in the Central Segment of South Atlantic: Insights from Numerical Modeling. *Acta Geol. Sin. Engl. Ed.* **2023**, *97*, 1229–1242. [[CrossRef](#)]
30. Sun, W.D. Initiation and evolution of the South China Sea: An overview. *Acta Geochim.* **2016**, *35*, 215–225. [[CrossRef](#)]
31. Li, C.F.; Xu, X.; Lin, J.; Sun, Z.; Zhu, J.; Yao, Y.J.; Zhao, X.X.; Liu, Q.S.; Kulhanek, D.K.; Wang, J.; et al. Ages and magnetic structures of the South China Sea constrained by deep tow magnetic surveys and IODP Expedition 349. *Geochem. Geophys. Geosystems* **2014**, *15*, 4958–4983. [[CrossRef](#)]
32. Sibuet, J.C.; Yeh, Y.C.; Lee, C.S. Geodynamics of the South China Sea. *Tectonophysics* **2016**, *692*, 98–119. [[CrossRef](#)]
33. Feng, X.L.; Zhang, G.C.; Wang, W.Y.; Zhao, Z.G.; Qiu, Z.Y.; Xie, X.J.; Ji, X.L.; Lu, B.L.; Song, S. An integrated study on distribution of Cenozoic basins in the South China Sea based on gravity, magnetic and seismic data. *Chin. J. Geophys.* **2018**, *61*, 4242–4254. (In Chinese) [[CrossRef](#)]
34. Li, Y.H.; Huang, H.B.; He, E.Y.; Cao, L.M.; Qiu, X.L.; Guo, X.W.; Liu, H.L. Tectonic framework of miniature continental block-narrow oceanic basin revealed by the southern typical profile in the China seas-Western Pacific Ocean. *Chin. J. Geophys.* **2020**, *63*, 1938–1958. (In Chinese) [[CrossRef](#)]
35. Safonova, I.; Maruyama, S. Asia: A frontier for a future supercontinent Amasia. *Int. Geol. Rev.* **2014**, *56*, 1051–1071. [[CrossRef](#)]
36. Ding, W.W.; Sun, Z.; Mohn, G.; Nirrengarten, M.; Tugend, J.; Manatschal, G.; Li, J.B. Lateral evolution of the rift-to-drift transition in the South China Sea: Evidence from multi-channel seismic data and IODP Expeditions 367&368 drilling results. *Earth Planet. Sci. Lett.* **2020**, *531*, 115932. [[CrossRef](#)]
37. Jian, Z.M.; Jin, H.Y.; Kaminski, M.A.; Ferreira, F.; Li, B.H.; Yu, P.S. Discovery of the marine Eocene in the northern South China Sea. *Natl. Sci. Rev.* **2019**, *6*, 881–885. [[CrossRef](#)] [[PubMed](#)]

38. Sun, Z.; Lin, J.; Qiu, N.; Jian, Z.M.; Wang, P.X.; Pang, X.; Zheng, J.Y.; Zhu, B.D. The role of magmatism in thinning and breakup of the South China Sea continental margin. *Natl. Sci. Rev.* **2019**, *6*, 871–876. [[CrossRef](#)] [[PubMed](#)]
39. Wessel, P.; Luis, J.F.; Uieda, L.; Scharroo, R.; Wobbe, F.; Smith, W.H.F.; Tian, D. The Generic Mapping Tools Version 6. *Geochem. Geophys. Geosystems* **2019**, *20*, 5556–5564. [[CrossRef](#)]
40. Tozer, B.; Sandwell, D.T.; Smith, W.H.; Olson, C.; Beale, J.R.; Wessel, P. Global Bathymetry and Topography at 15 Arc Sec: SRTM15+. *Earth Space Sci.* **2019**, *6*, 1847–1864. [[CrossRef](#)]
41. Lin, J.; Xu, Y.G.; Sun, Z.; Zhou, Z.Y. Mantle upwelling beneath the South China Sea and links to surrounding subduction systems. *Natl. Sci. Rev.* **2019**, *6*, 877–881. [[CrossRef](#)] [[PubMed](#)]
42. Wang, P.X. Tracing the life history of a marginal Sea—On the “South China Sea Deep” Research Program. *Chin. Sci. Bull.* **2012**, *57*, 1807–1826. [[CrossRef](#)]
43. Zhou, D.; Yao, B.C. Tectonics and sedimentary basins of the South China Sea: Challenges and progresses. *J. Earth Sci.* **2009**, *20*, 1–12. [[CrossRef](#)]
44. Li, Y.Q.; Abbas, A.; Li, C.F.; Sun, T.N.; Zlotnik, S.; Song, T.R.; Zhang, L.L.; Yao, Z.W.; Yao, Y.J. Numerical modeling of failed rifts in the northern South China Sea margin: Implications for continental rifting and breakup. *J. Asian Earth Sci.* **2020**, *199*, 104402. [[CrossRef](#)]
45. Tian, Z.X.; Yan, Y.; Huang, C.Y.; Dilek, Y.; Yu, M.M.; Liu, H.Q.; Zhang, X.C.; Zhang, Y. Fingerprinting Subducted Oceanic Crust and Hainan Plume in the Melt Sources of Cenozoic Basalts from the South China Sea Region. *Terra Nova* **2020**, *33*, 21–29. [[CrossRef](#)]
46. Xu, J.Y.; Avraham, Z.B.; Kelty, T.; Yu, H.S. Origin of marginal basins of the NW Pacific and their plate tectonic reconstructions. *Earth Sci. Rev.* **2014**, *130*, 154–196. [[CrossRef](#)]
47. Dong, D.D.; Qian, J.; Marta, P.G.; Lu, Z.J.; Luan, Y. Structural asymmetry of conjugate margins of the South China Sea and numerical modeling for its formation. *Mar. Sci.* **2014**, *38*, 136–141. (In Chinese) [[CrossRef](#)]
48. Gozzard, S.; Kusznir, N.; Franke, D.; Cullen, A.; Reemst, P.; Henstra, G. South China Sea crustal thickness and oceanic lithosphere distribution from satellite gravity inversion. *Pet. Geosci.* **2019**, *25*, 112–128. [[CrossRef](#)]
49. Ren, J.Y.; Luo, P.; Gao, Y.Y.; Wang, H.J.; Lei, C.; Chao, P. Structural, Sedimentary and Magmatic Records during Continental Breakup at Southwest Sub-Basin of South China Sea. *Earth Sci.* **2022**, *47*, 2287–2302. (In Chinese) [[CrossRef](#)]
50. Zhao, Z.X.; Sun, Z.; Qiu, N.; Zhao, M.H.; Zhang, J.Z.; Li, F.C.; Lin, J.; Lee, E.Y. The paleo-lithospheric structure and rifting-magmatic processes of the northern South China Sea passive margin. *Gondwana Res.* **2023**, *120*, 162–174. [[CrossRef](#)]
51. Liu, C.; Li, J.H.; Wang, Z.C. Dynamic model analysis of formation and evolution of the South China Sea. *Geoscience* **2023**, *7*, 259–269. (In Chinese) [[CrossRef](#)]
52. Maus, S.; Barckhausen, U.; Berkenbosch, H.; Bournas, N.; Brozena, J.; Childers, V.; Dostaler, F.; Fairhead, J.D.; Finn, C.; von Frese, R.R.B.; et al. EMAG2: A 2-arc min resolution Earth Magnetic Anomaly Grid compiled from satellite, airborne, and marine magnetic measurements. *Geochem. Geophys. Geosystems* **2009**, *10*, 1–12. [[CrossRef](#)]
53. Zhang, J.; Yang, G.L.; Tan, H.B.; Wu, G.J.; Wang, J.P. Mapping the Moho depth and ocean-continent transition in the South China Sea using gravity inversion. *J. Asian Earth Sci.* **2021**, *218*, 104864. [[CrossRef](#)]
54. Guan, Q.S.; Zhang, T.; Taylor, B.; Gao, J.Y.; Li, J.B. Ridge jump reorientation of the South China Sea revealed by high-resolution magnetic data. *Terra Nova* **2021**, *33*, 475–482. [[CrossRef](#)]
55. Chang, S.P.; Pubellier, M.; Delescluse, M.; Qiu, Y.; Nirrengarten, M.; Mohn, G.; Chamot-Rooke, N.; Liang, Y. Crustal architecture and evolution of the southwestern South China Sea: Implications to continental breakup. *Mar. Pet. Geol.* **2022**, *136*, 105450. [[CrossRef](#)]
56. Peng, X.; Li, C.F.; Shen, C.B.; Li, K.; Zhao, Z.G.; Xie, X.J. Anomalous lower crustal structure and origin of magmatism in the southeastern margin of the South China Sea. *Mar. Pet. Geol.* **2020**, *122*, 104711. [[CrossRef](#)]
57. Gao, J.W.; Wu, S.G.; Lüdmann, T.; Li, C.F.; Li, L.; Lu, Y.T.; Yang, Z.L.; Tian, L.Y.; Qin, Y.P.; Song, T.R. Extensional structures and Cenozoic magmatism in the northwestern South China Sea. *Gondwana Res.* **2023**, *120*, 219–234. [[CrossRef](#)]
58. Gerya, T.; Yuen, D.A. Characteristics-based marker-in-cell method with conservative finite-differences schemes for modeling geological flows with strongly variable transport properties. *Phys. Earth Planet. Inter.* **2003**, *140*, 293–318. [[CrossRef](#)]
59. Gerya, T. *Introduction to Numerical Geodynamic Modelling*; Cambridge University Press: Cambridge, UK, 2019. [[CrossRef](#)]
60. Schubert, G.; Turcotte, D.L.; Olson, P. *Mantle Convection in the Earth and Planets*; Cambridge University Press: Cambridge, UK, 2001. [[CrossRef](#)]
61. Clauser, C.; Huenges, E. *Thermal Conductivity of Rocks and Minerals*; American Geophysical Union (AGU): Washington, DC, USA, 1995. [[CrossRef](#)]
62. Ranalli, G.; Rybach, L. Heat flow, heat transfer and lithosphere rheology in geothermal areas: Features and examples. *J. Volcanol. Geotherm. Res.* **2005**, *148*, 3–19. [[CrossRef](#)]
63. Zhang, J.J.; Shang, S.; Wei, C.J.; Zhang, N.; Zhang, G.W.; Jin, Z.M.; Zhang, J.F.; Cao, S.Y.; Liu, J.L.; Liu, Y.J. Present Status and Development Prospect of Studies of Rheology of Continental Lithosphere. *Acta Geosci. Sin.* **2019**, *40*, 9–16. (In Chinese) [[CrossRef](#)]
64. Ranalli, G. Rheology of the Earth. *Tectonophysics* **1995**, *269*, 347–349. [[CrossRef](#)]
65. Gerya, T.V.; Yuen, D.A. Robust characteristics method for modelling multiphase visco-elasto-plastic thermo-mechanical problems. *Phys. Earth Planet. Inter.* **2007**, *163*, 83–105. [[CrossRef](#)]
66. Burov, E.; Poliakov, A. Erosion and rheology controls on synrift and postrift evolution: Verifying old and new ideas using a fully coupled numerical model. *J. Geophys. Res. Solid Earth* **2001**, *106*, 16461–16481. [[CrossRef](#)]

67. Lu, B.L.; Wang, W.Y.; Zhao, Z.G.; Feng, X.L.; Zhang, G.C.; Luo, X.G.; Yao, P.; Ji, X.L. Characteristics of deep structure in the South China Sea and geological implications: Insights from gravity and magnetic inversion. *Chin. J. Geophys.* **2018**, *61*, 4231–4241. (In Chinese) [[CrossRef](#)]
68. Qian, K.; Yan, Y.; Huang, Q.Y.; Chen, W.H.; Yu, M.M.; Tian, Z.X. Sea Floor Spreading of South China Sea and Its Depositional Records of Sea and Land Changes. *Mar. Geol. Front.* **2016**, *32*, 10–23. (In Chinese) [[CrossRef](#)]
69. Zhang, G.C.; Jia, Q.J.; Wang, W.Y.; Wang, P.J.; Zhao, Q.L.; Sun, X.M.; Xie, X.J.; Zhao, Z.; Tang, W. On tectonic framework and evolution of the South China Sea. *Chin. J. Geophys.* **2018**, *61*, 4194–4215. (In Chinese) [[CrossRef](#)]
70. Li, Z.K.; Li, C.F.; Zhu, S.; Huang, L.; Liu, W.X. High-resolution effective elastic thicknesses of the lithosphere in the South China Sea and their controlling factors. *Acta Geol. Sin.* **2022**, *96*, 2670–2682. [[CrossRef](#)]
71. Zheng, J.Y.; Dai, Y.D.; Liu, J.; Pang, X.; Ren, J.Y.; Dong, M. Differences in continental crust structure and its extensional fracture process in northern South China Sea. *J. Yangtze Univ. Nat. Sci. Ed.* **2022**, *19*, 12–22. (In Chinese) [[CrossRef](#)]
72. Ren, J.Y.; Pang, X.; Yu, P.; Lei, C.; Luo, P. Characteristics and formation mechanism of deepwater and ultra-deepwater basins in the northern continental margin of the South China Sea. *Chin. J. Geophys.* **2018**, *61*, 4901–4920. (In Chinese) [[CrossRef](#)]
73. Zhang, J.; Xiong, L.P.; Wang, J. Characteristics and Mechanism of Geodynamic evolution of the South China Sea. *Chin. J. Geophys.* **2001**, *44*, 602–610. (In Chinese) [[CrossRef](#)]
74. Zhang, N.; Li, Z. Formation of mantle “lone plumes” in the global downwelling zone—A multiscale modelling of subduction-controlled plume generation beneath the South China Sea. *Tectonophysics* **2018**, *723*, 1–13. [[CrossRef](#)]
75. Li, F.C.; Sun, Z.; Pang, X.; Liao, J.; Yang, H.F.; Xie, H.; Zhuo, H.T.; Zhao, Z.X. Low-Viscosity Crustal Layer Controls the Crustal Architecture and Thermal Distribution at Hyperextended Margins: Modeling Insight and Application to the Northern South China Sea Margin. *Geochem. Geophys. Geosystems* **2019**, *20*, 3248–3267. [[CrossRef](#)]
76. Cramer, F.; Tackley, P.; Meilick, I.; Gerya, T.; Kaus, B. A free plate surface and weak oceanic crust produce single-sided subduction on Earth. *Geophys. Res. Lett.* **2012**, *39*, 1–7. [[CrossRef](#)]
77. Xin, Y.F.; Yan, Y.; Marta, P.G.; Luo, Y. Impact of Extension Rate and Crustal Rheology on the Evolution of Passive Continental Margins. *Geotecton. Metallog.* **2022**, *46*, 191–201. (In Chinese) [[CrossRef](#)]
78. Burov, E. Rheology and strength of the lithosphere. *Mar. Pet. Geol.* **2011**, *28*, 1402–1443. [[CrossRef](#)]
79. Dymkova, D.; Gerya, T.; Burg, J. 2D thermomechanical modelling of continent–arc–continent collision. *Gondwana Res.* **2016**, *32*, 138–150. [[CrossRef](#)]
80. Hung, T.D.; Yang, T.; Le, B.M.; Yu, Y.Q.; Xue, M.; Liu, B.H.; Liu, C.G.; Wang, J.; Pan, M.H.; Huong, P.T.; et al. Crustal Structure Across the Extinct Mid-Ocean Ridge in South China Sea from OBS Receiver Functions: Insights Into the Spreading Rate and Magma Supply Prior to the Ridge Cessation. *Geophys. Res. Lett.* **2021**, *48*, e2020GL089755. [[CrossRef](#)]
81. Barckhausen, U.; Engels, M.; Franke, D.; Ladage, S.; Pubellier, M. Evolution of the South China Sea: Revised ages for breakup and seafloor spreading. *Mar. Pet. Geol.* **2014**, *58*, 599–611. [[CrossRef](#)]
82. Yu, J.H.; Yan, P.; Qiu, Y.; Delescluse, M.; Huang, W.K.; Wang, Y.L. Oceanic crustal structures and temporal variations of magmatic budget during seafloor spreading in the East Sub-basin of the South China Sea. *Mar. Geol.* **2021**, *436*, 106475. [[CrossRef](#)]
83. Sun, Z.; Li, F.C.; Lin, J.; Sun, L.T.; Pang, X.; Zheng, J.Y. The Rifting-Breakup Process of the Passive Continental Margin and Its Relationship with Magmatism: The Attribution of the South China Sea. *Earth Sci.* **2021**, *46*, 770–789. (In Chinese) [[CrossRef](#)]
84. Ren, J.Y.; Pang, X.; Lei, C.; Yuan, L.Z.; Liu, J.; Yang, L.L. Ocean and continent transition in passive continental margins and analysis of lithospheric extension and breakup process: Implication for research of the deepwater basins in the continental margins of South China Sea. *Earth Sci. Front.* **2015**, *22*, 102–114. (In Chinese) [[CrossRef](#)]
85. Manatschal, G. New models for evolution of magma-poor rifted margins based on a review of data and concepts from West Iberia and the Alps. *Int. J. Earth Sci.* **2004**, *93*, 432–466. [[CrossRef](#)]
86. Manatschal, G.; Sauter, D.; Karpoff, A.M.; Masini, E.; Mohn, G.; Lagabrielle, Y. The Chenaillet Ophiolite in the French/Italian Alps: An ancient analogue for an Oceanic Core Complex? *Lithos* **2011**, *124*, 169–184. [[CrossRef](#)]
87. Zhang, C.M.; Sun, Z.; Manatschal, G.; Pang, X.; Li, S.Z.; Sauter, D.; Peron-Pinvidic, G.; Zhao, M.H. Ocean-continent transition architecture and breakup mechanism at the mid-northern South China Sea. *Earth-Sci. Rev.* **2021**, *217*, 103620. [[CrossRef](#)]
88. Luo, P.; Manatschal, G.; Ren, J.Y.; Zhao, Z.G.; Wang, H.J.; Tong, D.J. Tectono-Magmatic and stratigraphic evolution of final rifting and breakup: Evidence from the tip of the southwestern propagator in the South China Sea. *Mar. Pet. Geol.* **2021**, *129*, 105079. [[CrossRef](#)]
89. Qian, S.P.; Gazel, E.; Nichols, A.R.; Cheng, H.; Zhang, L.; Salters, V.J.; Li, J.; Xia, X.P.; Zhou, H.Y. The Origin of Late Cenozoic Magmatism in the South China Sea and Southeast Asia. *Geochem. Geophys. Geosystems* **2021**, *22*, e2021GC009686. [[CrossRef](#)]
90. Zhu, W.J.; Du, X.X.; Shang, L.N.; Li, P.F.; Pan, J.; Qi, J.H.; Meng, Y.K.; Hu, G. Spatiotemporal heterogeneity of the conjugate continental margin evolution in the South China Sea and future ocean drilling wells. *Mar. Geol. Quat. Geol.* **2022**, *42*, 110–123. (In Chinese) [[CrossRef](#)]
91. Nirrengarten, M.; Mohn, G.; Kusznir, N.J.; Sapin, F.; Despinois, F.; Pubellier, M.; Chang, S.P.; Larsen, H.C.; Ringenbach, J.C. Extension modes and breakup processes of the southeast China-Northwest Palawan conjugate rifted margins. *Mar. Pet. Geol.* **2020**, *113*, 104123. [[CrossRef](#)]
92. Bird, P. An updated digital model of plate boundaries. *Geochem. Geophys. Geosystems* **2003**, *4*, 1–52. [[CrossRef](#)]
93. Zhao, C.J.; Yu, P.; Zhang, L.L.; Guan, X.F. Three-dimensional magnetic structure and genesis of the oceanic crust of the northern South China Sea. *J. Asian Earth Sci.* **2020**, *204*, 104568. [[CrossRef](#)]

94. Shi, H.S.; Li, C.F. Mesozoic and early Cenozoic tectonic convergence-to-rifting transition prior to opening of the South China Sea. *Int. Geol. Rev.* **2012**, *54*, 1801–1828. [[CrossRef](#)]
95. Yeh, Y.C.; Sibuet, J.C.; Hsu, K.H.; Liu, C.S. Tectonic evolution of the Northeastern South China Sea from seismic interpretation. *J. Geophys. Res.* **2010**, *115*, 1–21. [[CrossRef](#)]

Disclaimer/Publisher’s Note: The statements, opinions and data contained in all publications are solely those of the individual author(s) and contributor(s) and not of MDPI and/or the editor(s). MDPI and/or the editor(s) disclaim responsibility for any injury to people or property resulting from any ideas, methods, instructions or products referred to in the content.